A Fully Coupled Fluid-Structure Interaction Model of the Secondary Lymphatic Valve

John T. Wilson[1], Lowell T. Edgar[1], Saurabh Prabhakar[2], Marc Horner[3], Raoul van Loon[4], James E. Moore, Jr.[1]*

[1]Department of Bioengineering
Imperial College London
South Kensington Campus
London, SW7 2AZ, UK

[2]ANSYS Software Private Ltd.
34/01, Rajiv Gandhi Infotech Park,
MIDC, Hinjawadi
Pune 411057
India

[3]ANSYS, Inc.
1007 Church Street, Suite 250
Evanston, IL 60201
USA

[4]Zienkiewicz Centre of Computational Engineering
College of Engineering
Swansea University
Singleton Park
Swansea, SA2 8PP, UK

*Corresponding author. Tel: +44 (0)20-75 945179; fax: +44 (0)20-75 94-9817.
E-mail address: james.moore.jr@imperial.ac.uk (J.E. Moore, Jr.)

Keywords: Fluid-structure interactions; Fully coupled FSI; Lymphatic system; Lymphatic valve; Lymphatic flow; Flow resistance

Revision 1, *Computer Methods in Biomechanics and Biomedical Engineering*, 04/08/2018

Abstract

The secondary lymphatic valve is a bi-leaflet structure frequent throughout collecting vessels that serves to prevent retrograde flow of lymph. Despite its vital function in lymph flow and apparent importance in disease development, the lymphatic valve and its associated fluid dynamics have been largely understudied. The goal of this work was to construct a physiologically relevant computational model of an idealized rat mesenteric lymphatic valve using fully coupled fluid-structure interactions to investigate the relationship between three-dimensional flow patterns and stress/deformation within the valve leaflets. The minimum valve resistance to flow, which has been shown to be an important parameter in effective lymphatic pumping, was computed as 268 g/mm^4-s. Hysteretic behavior of the lymphatic valve was confirmed by comparing resistance values for a given transvalvular pressure drop during opening and closing. Furthermore, eddy structures were present within the sinus adjacent to the valve leaflets in what appear to be areas of vortical flow; the eddy structures were characterized by non-zero velocity values (up to ~ 4 mm/s) in response to an applied unsteady transvalvular pressure. These modeling capabilities present a useful platform for investigating the complex interplay between soft tissue motion and fluid dynamics of lymphatic valves and contribute to the breadth of knowledge regarding the importance of biomechanics in lymphatic system function.

Introduction

The lymphatic system is responsible for the transport of lymph from the tissue interstitial space to the venous return (Swartz and Skobe 2001). In addition to maintaining tissue homeostasis, the lymphatic system is also vital in immune cell trafficking, cerebrospinal fluid/nasal drainage, and lipid transport (Zawieja et al. 2011). Decreased lymphatic pumping and flow can result in a condition known as lymphedema, which results in an excess of fluid in the interstitium

(Mortimer and Rockson 2014). Lymphedema is a debilitating disease that affects many patients who have undergone axillary lymph node dissection as part of their breast cancer therapy (Cariati et al. 2015). Currently, there is no cure for lymphedema and management of the disease includes physical therapy and compression bandages/garments (Gordon and Mortimer 2007).

Solutes and fluid passively enter the lymphatic system through initial lymphatic vessels which eventually give rise to the collecting lymphatics, which differ from initial lymphatics in size as well as the presence of lymphatic muscle cells (LMCs) and secondary valves (Zawieja, von der Weid and Gashev 2011). The secondary lymphatic valves are bi-leaflet structures that serve to prevent retrograde flow. The leaflets consist of lymphatic endothelial cells (LECs) (Takada 1971, Vajda and Tomcsik 1971) with an extracellular matrix (ECM) composed of elastin and are almost entirely devoid of collagen (Rahbar et al. 2012). The valves are frequent throughout collecting vessels and function in a complex mechanical environment where the valve deflections are determined by fluid pressures upstream and downstream of the valve. Further, the forkhead transcription factor FOXC2 is highly expressed in LECs of the valve sinus where others have proposed the existence of complex flow patterns (Mellor et al. 2007, Sabine et al. 2015).

Despite its vital function in lymphatic function and role in disease development, few experimental studies have attempted to investigate the fluid dynamics at the secondary valve. Davis et al. investigated the relationship between the pressure gradient required to open or close a valve and vessel distension (Davis et al. 2011). They found that a pressure difference around 10 Pa was required to open or close the valve at low transmural pressures. However, as the vessel became distended, a much larger pressure gradient was required to close the valve (~225 Pa) than was required to open the valve (~60 Pa), suggesting the valve is biased to the open position. These experimental data were later used to estimate valve resistance to favorable

pressure differences (Bertram et al., 2012), but there was a high degree of uncertainty in the estimations due to the small quantities involved (pressure differences < 0.2 cm H_2O, flow rates < 20 μl/min, diameters < 250 μm). Valve resistance to favorable pressure is one of the most important parameters in determining the effectiveness of lymphatic pumping (Jamalian et al., 2013). Recently, Margaris et al. used micro-particle image velocimetry to study flow within the bicuspid lymphatic valves and observed eddies around the valve leaflets (Margaris et al. 2016). While they were able to quantitatively resolve secondary flows within the valve region, the experiments were not extended to three-dimensional (3D) analysis, which limited the characterization of the flow field. Reported efforts to model lymphatic valves computationally in 3D are also few in number. Our group modeled flow in a static lymphatic valve with the goal of understanding nitric oxide concentration fields (Wilson et al. 2013). We have since studied valve resistance using an uncoupled fluid-structure interaction approach (Wilson et al. 2015). Macdonald et al. developed a two-dimensional (2D) model of a secondary valve where motion of the valve was imposed rather than solved by a fluid-structure interaction (FSI) approach (Macdonald 2008).

While these previous studies provided insight into the flow patterns around lymphatic valves, there is still a need for a more accurate description of valve resistance to favorable and adverse pressure differences, since this is a primary determinant of lymphatic pumping. This requires taking into account the strong coupling between the solid leaflets and lymph flow. Fully coupled simulations have provided beneficial insight into heart valve dynamics (Chandran and Vigmostad 2013), but these techniques have never been applied to lymphatic valves. Valve leaflets are generally considered passive structures as they are composed entirely of elastin and endothelial cells (Mazzoni et al. 1987, Rahbar, Weimer, Gibbs, Yeh, Bertram, Davis, Hill, Zawieja and Moore Jr 2012), and their movement is thus primarily determined by differential pressure across the valve .Thus, the goal of this work was to construct a

physiologically relevant computational model using a fully coupled FSI approach to simulate the 3D flow patterns around the deflecting lymphatic valve, providing a more accurate estimate of valve resistance.

Methods

Lymphatic Vessel and Valve Geometry

We constructed an idealized geometric 3D representation of a rat mesenteric lymphatic valve using SolidWorks 2014 (Dassault Systèmes Solidworks Corp, Waltham, MA, USA) (Fig. 1 A). This previously described geometry consisted of two identical valve leaflets fixed at the annuli encapsulated within a bulbous sinus region (Wilson, van Loon, Wang, Zawieja and Moore 2015). Two straight tube extensions were added at the inlet and outlet of the sinus to aid in the application of boundary conditions, resulting in a total axial length of 700 μm. Specifically, the extended inlet would allow for flow to fully develop upstream of the valve and extending the outlet would minimize numerical interference of the outlet boundary condition with flow in the physiologic domain of interest. Geometric dimensions are reported in Table 1. The global coordinate system was defined with the *z*-axis aligned with the vessel centerline, the *x*-axis spanning the major axis of the elliptical orifice of the valve, and the *y*-axis spanning the minor axis of the orifice (Fig. 1 A). The leaflet thickness, *h*, was a constant value of 5 μm, and the distance between the two leaflet tips (i.e., the minor axis of the elliptical orifice), d_o, was 10 μm. Although real valve leaflets are generally not symmetric, the model was designed with symmetric leaflets to reduce computational demands. Only ¼ of the full geometry was simulated by applying symmetry at the *xz*-plane and the *yz*-plane, with the leaflets partially open (d_o =10 μm) in the stress-free state (Fig. 1 A). This initial state of the valve leaflets agrees with the literature, which suggests the leaflets to be biased to the open position (Davis, Rahbar, Gashev, Zawieja and Moore 2011). The geometry was imported into ANSYS 16.1 (ANSYS,

Inc., Canonsburg, PA, USA) to create the computational meshes for the fluid and solid domain and to perform the simulations (Fig. 1 B).

FSI Overview

The FSI capabilities within the commercial software package ANSYS were used to perform the simulations. There were two mesh domains: one for the fluid domain (lymph) and one for the solid domain (valve leaflet). The fluid domain was discretized using an arbitrary Lagrangian-Eulerian (ALE) description which involved a moving grid that was updated at each time-step to conform to the moving leaflet boundary. Use of the ALE description allows for both precise calculation of the displacing leaflet surfaces as well as computation of wall shear-stress (WSS) on the leaflets during the simulation.

To ensure a strong fluid-structure coupling, a two-way iterative method was employed using ANSYS Fluent as the fluid solver and ANSYS Mechanical APDL as the structural solver. Within each time step, the fluid and solid equations were solved separately; force data were transferred from the fluid to the solid and displacement data from the solid to the fluid until convergence was reached. Flow convergence was assumed when flow variables of interest (flow rate at the outlet and force along the leaflet surface) reached a steady-state value within a time-step. The normalized residual for the continuity equation in the pressure-based solver dropped two orders of magnitude, while the normalized residuals for the momentum equations dropped by six orders of magnitude. The fluid mesh was updated to conform to the moving solid boundary at each time-step.

Fluid Domain

The viscous form of the Navier-Stokes equations was used to solve the laminar fluid flow problem. Lymph was assumed to be an incompressible Newtonian fluid with a density ρ_f of 1.0 g/cm^3 and dynamic viscosity μ_f of 1.5 cP (Swartz and Fleury 2007). A time-varying pressure waveform was applied at the inlet (Fig. 1 C). While this waveform is idealized, the

peak pressure of 60 Pa, time-averaged value of 33 Pa, and period of 1.75 s, are typical of pressures and time scales obtained from physiologic experiments with pressure-loaded rat mesenteric lymphatic vessels (Benoit et al. 1989, Davis, Rahbar, Gashev, Zawieja and Moore 2011). The outlet pressure was set to 0 Pa throughout the simulation. The resulting Reynolds numbers were less than 2 when using these settings, justifying the initial assumption of laminar flow. Leaflet surfaces in contact with the fluid domain were treated as fluid-structure interfaces. The interface was stabilized using a boundary source coefficient that scales the diagonal components of the discretized continuity equation. The vertical and horizontal lines in the 'down-the-barrel' view of the geometry (Fig. 1, upper right) represent symmetry boundary conditions applied within the fluid domain. The flow waveform was discretized using a time step of 3 ms (Fig. 1 C). An under-relaxation algorithm was applied to the force being transferred from the fluid solver to the structural solver to further stabilize the solution by limiting the potentially large variation in data transfer between successive iterations.

Fluid Computational Mesh and Remeshing Scheme

The fluid problem was solved using the PISO solution scheme and spatial discretization schemes of least squared cell based, second order, and second order upwinding for the spatial discretization of gradient, pressure, and momentum, respectively. The fluid domain was meshed using 156,500 volumetric tetrahedral elements, with a characteristic element length of 10.2 μm. The fluid mesh was refined in the region between the valve leaflets where central lymph flow occurs because these elements were expected to stretch during opening. A sensitivity analysis of the fluid mesh was performed by comparing WSS values on the belly of the leaflet for meshes with 156,042 cells and 423,075 cells, which were subjected to the peak inlet pressure obtained from the waveform boundary condition (Fig. 1 C). The disparity between the two meshes was less than 7 % in normalized root-mean-squared error (NRMSE) across a range of sampling locations and less than 5 % in the peak WSS value at the trailing

edge of the leaflet. Therefore, we determined that the 156,042 element fluid mesh was sufficient to meet the goals of this study.

Diffusion-based smoothing was implemented to allow nodes in the fluid mesh to adjust the motion of the moving leaflet boundary whilst minimizing the effects on mesh quality. To circumvent severe cell quality deterioration and prevent degenerate cells, local cell and local face remeshing methods were used. At each time-step, once the fluid mesh update occurs based on displacement data received from the structural simulation, ANSYS Fluent agglomerates a selection of cells based on size and skewness criteria (Table 2) and locally remeshes the agglomerated cells and their faces. The mesh was updated if the new cells and faces satisfied the quality criteria (with the solution mapped from the old to the new mesh). Otherwise, the new mesh was discarded and the old one retained. Simulations were stopped just short of leaflet contact in order to avoid numerous numerical issues associated with contact such as increased pressure gradients, element distortion and significant changes in mesh connectivity and topology, and greatly increased computational demand.

Solid Domain

The valve leaflet was meshed with 3,149 tetrahedral elements using the SOLID187 element, which is a 3D 10-noded element well-suited to modelling irregular meshes and allows for quadratic behavior. The solid domain was assigned a neo-Hookean model with a value of 20 kPa for the shear modulus *G*, which is slightly lower than that of arterial elastin (Mithieux and Weiss 2005, Nivison-Smith and Weiss 2011, Zou and Zhang 2009), and a value of 193.3 kPa for the bulk modulus *K* assuming a nearly incompressible Poisson's ratio of 0.45. The solid material density ρ_s was set to 1080 kg/m^3, a commonly used density value for aortic valve leaflets (Cao et al. 2015, Lantz et al. 2011, Marom et al. 2012).

Results

The increasing pressure applied at the inlet resulted in deflection (i.e., displacement of the leaflet tip) predominantly in the *y*-direction, increasing the minor axis of the elliptical orifice and permitting increased flow through the valve (Fig. 2). Flow was well within the laminar region with a maximum Reynolds number Re = 1.98. An eddy-like structure was observed adjacent to the valve leaflets near the sinus wall, becoming more prominent near peak flow when the deflection is highest (Fig. 2). Positive and negative principal strain within the leaflet was concentrated along the yz-symmetry plane where deflection was the highest and along the boundary with the vessel wall (Fig. 3 A B). The reconstructed full-geometry of the valve leaflets provides the shape of the opened lymphatic valve, demonstrating that maximum displacement of the leaflets occurred at the center of the valve along the yz-symmetry plane (Fig. 3 C). While the peak pressure of the waveform applied at the inlet occurred at 0.75 s, the deflection reached a maximum of 27.19 μm slightly later at 0.764 s (Fig. 3 D). The minimum deflection of -0.37 μm occurred at 1.656 s, with a corresponding pressure across the valve region of -4.26 Pa. There was less deflection for a given transvalvular pressure (i.e., the pressure difference between the inlet and outlet) during opening of the valve compared to closing (Fig. 3 E). As an example, for an imposed transvalvular pressure of 30 Pa (occurring at time 0.252 and 1.25 s), the valve leaflet deflection was lower during opening at 10.52 μm (0.252 s) compared to 16.86 μm during closing (1.25 s).

Adopting cardiac terminology, the magnitude of flow velocity increased from early systole (0.009 s) through mid-systole (0.25 s) until reaching a maximum at peak systole (0.75 s), then decreased until reversing direction at late systole (1.25 s) until early diastole (1.65 s) (Fig. 4). The maximum flow rate occurred at peak pressure, reaching 792 μL/hr at 0.75 s. Between early systole (0.009 s) and mid-systole (0.25 s) the positive transvalvular pressure induced partial opening of the leaflets during which period the free edges of the leaflets remained tangential to axial lymph flow. By peak systole (0.75 s), the leaflets were pushed

towards the lymphatic sinus wall by the increased transvalvular pressure and the flow rate reached a maximum shortly afterwards. Throughout the entire cycle, an eddy structure was present within the sinus adjacent to the valve leaflets (Fig. 4).

At peak systole, velocities up to approximately 4 mm/s contributed to reversed flow within these areas of disturbed flow near the sinus wall. Computations of the *y*-velocity component (the primary direction of leaflet deflection), indicate flow in the opposing direction of net leaflet deflection (Fig. 5 A). Similarly, the negative axial velocities reached -0.41 mm/s within the sinus region above the valve leaflets at peak systole (Fig. 5 B).

The magnitude of WSS distributions at the leaflet surface exposed to central lymph flow was also computed (Fig. 6). During early systole (0.009 s), nearly stagnant flow and low pressures subjected the leaflet to a uniform and low-magnitude WSS profile. By mid-systole, the leaflets began to experience much higher values of WSS concentrated at the free edge of the leaflet (~160 dyne/cm^2). It should be noted that the peak values of WSS occurred over a very small surface at the leaflet tip, and shear stress values were generally between 20 and 100 dyne/cm^2 across the leaflet surface at peak systole.

The forward flow resistance, R_f, was computed as the difference between the surface-averaged pressure upstream (where the valve first contacts the annulus at the insertion site, Fig. 1) and downstream of the valve (where the curvature of the sinus ends, Fig. 1) divided by the flow rate. During valve opening, the resistance decreased from 1801 g/mm^4-s to 268 g/mm^4-s at 0.846 s (Fig. 7 A red curve). The resistance increased to 1850 g/mm^4-s as the valve closed (Fig. 7 A blue curve). Although the minimum resistance occurred at 0.846 s, resistance changed very little between 0.4 s and 1.1 s, at which point the valve can be considered to be fully ‘open’ (Fig. 7 B). The corresponding pressure value at these time points that represent the end of opening and start of closing of the valve was roughly 44.5 Pa. Similar to the deflection versus pressure data, there was an apparent hysteretic behavior in the valve resistance as R_f was

generally higher during opening (red curve) compared to closing (blue curve) for a given ΔP (see Fig. 7 B). Note that we primarily focused on resistance to forward flow in this study, but did calculate resistance during reverse flow due to the negative pressure gradient occurring after 1.5 s.

Discussion

We performed a fully coupled transient simulation of flow through a lymphatic valve describing the interaction between the fluid flow and the deforming valve leaflet. This study allowed us to characterize the fluid dynamics within the sinus, the deflection of the valve leaflets, and the resistance to favorable pressure. The results presented in this study clearly demonstrate the regional complexity of flow within the lymphatic sinus as well as the hysteretic behavior of valve opening and closing. For example, non-zero velocity magnitudes (up to ~ 4 mm/s) can be observed along the instantaneous streamlines contributing to the flow eddies within the sinus region (Fig. 4), and we found that lymph experienced more resistance to favorable pressure during valve opening versus closing (Fig. 7).

Few experimental studies have quantified the flow field within the collecting lymphatic vessels. Dixon and colleagues acquired images using a high speed camera and used lymphocytes as tracers assuming fully developed laminar flow (Dixon et al. 2007, Dixon et al. 2006, Dixon et al. 2005) and found lymphocyte velocities vary in both phase and magnitude with an average of 0.87 ± 0.18 and peaks of 2.2 – 9.0 mm/s. Consequently, this resulted in an average shear stress of 0.64 ± 0.14 dyne/cm^2 with peaks of 4 – 12 dyne/cm^2 (Dixon, Greiner, Gashev, Cote, Moore Jr and Zawieja 2006). Our results, which resolve velocity at a much smaller length scale, indicate higher velocity magnitudes at the trailing edge of the leaflets (44 mm/s at peak systole, t = 0.75 s). The WSS values in this study were also higher, with peak values in excess of 80 dyne/cm^2. The relatively high values of WSS captured in this FSI model

are not surprising given the converging orifice shape of the valve opening. The flow characteristics featured here qualitatively match those obtained by Margaris et al (Margaris, Nepiyushchikh, Zawieja, Moore Jr and Black 2016). Specifically, both studies identified eddies adjacent to the valve leaflets near the sinus wall. While Margaris and colleagues were limited to capturing the flow at one plane within the vessel, our present model complements this work by resolving the full flow field in 3D. Interestingly, the FSI model indicated non-zero velocity magnitudes (up to ~ 4 mm/s) along instantaneous streamlines contributing to the flow eddies; such non-zero velocities at the flow eddies were not described by Margaris and colleagues. Further, at a cross-sectional area just downstream of the trailing edges of the leaflets during the maximum pressure differential, negative velocity components with magnitudes similar to those in the bulk lymph flow were observed below the valve leaflets where flow was projecting vertically (i.e., *y*-direction) away from the leaflets (Fig. 5 B). This may be attributed to the solid leaflet 'squeezing' the fluid in this direction.

Leaflet deflection reached a maximum and resistance to favorable pressure reached a minimum at an applied transvalvular pressure difference of approximately 44.5 Pa, at which point the valve can be considered fully opened. After the valve was opened, pressure decreased until deflection reached a minimum of -0.37 μm at 1.656 s. The corresponding pressure difference directly upstream and downstream of the valve region at this time point is -4.2 Pa, which implies a pressure drop of 48.7 Pa was required to bring the valve from fully open to mostly closed. Note that we halted the simulation prior to full closure of the valve, as this would require a complex contact algorithm for the solid mesh and would cause problems with element skewness and connectivity in the fluid mesh. Experiments performed by Davis and colleagues (Davis, Rahbar, Gashev, Zawieja and Moore 2011) and interpreted by Bertram et al (Bertram et al. 2014) indicate the pressure required to close the valve varied from roughly 14 to 200 Pa, depending on the baseline transmural pressure applied to the lymphatic vessel *ex vivo*. Our

prediction of 48.7 Pa to close the valve falls within this range. Future simulations should further investigate the conditions required for full valve closure, as well as the interplay with transmural pressure, wall compliance, and active contraction by LMCs.

We calculated the minimum valve resistance to flow at 268 g/mm^4-s, which is within the same order of magnitude of calculations from our previous work using an uncoupled approach (119 g/mm^4-s) (Wilson, van Loon, Wang, Zawieja and Moore 2015) and the value estimated from experimental data by Bertram et al (60 g/mm^4-s) (Bertram, Macaskill, Davis and Moore Jr 2014). Given that our simulation involved the complete 3D geometry of the valve region as well as fully coupled FSI, we believe that our current model gives the most accurate prediction of minimal valve resistance to date, and it would appear that simpler methods tended to underestimate this resistance. The minimum resistance of the valve has been shown to dramatically affect pumping efficiency in the lymphatic system (Bertram, Macaskill, Davis and Moore Jr 2014, Jamalian et al. 2013). We have previously modeled the secondary lymphatic valve using an uncoupled FSI approach, and the major difference in this work compared to the uncoupled model is that the force applied to the leaflets is non-uniform in fully coupled FSI (as opposed to a uniform force in the uncoupled model). This presumably results in a more accurate estimation of the geometrically-dependent resistance to favorable pressure, although it is currently not possible to confirm this experimentally.

Another important behavior noted in the experiments by Davis et al. was that when transmural pressure was positive and the valve was exposed to a slightly adverse pressure difference, the leaflets remained open (Davis, Rahbar, Gashev, Zawieja and Moore 2011). The leaflets did not close until the pressure drop was considerably adverse, indicating the valve is biased towards the open configuration. It was also observed that, for a given transmural pressure, the favorable transvalvular pressure difference required to open a previously closed valve was less in magnitude than the adverse transvalvular pressure difference required to close

it. This difference increased with transmural pressure, presumably because the leaflets were spread further apart. The present model also exhibits bias between opening and closing, in that a larger pressure was required to close the valve to a given deflection in the cycle than to open it to that same deflection. This phenomenon can be observed in the tip deflection data, in which we found that the same pressure difference resulted in more deflection while closing than during opening (Fig. 3 E). Our simulations also reveal a bias in the flow resistance that results from differences in leaflet deflections in opening versus closing. For a given ΔP, R_f was higher during opening (Fig. 7 B red curve) compared to closing (Fig. 7 B blue curve). The difference in resistance for a given ΔP can be attributed to a larger orifice area of the valve during the closing process compared to opening. This bias could not have been observed experimentally due to the swiftness of valve opening/closing, compounded with the difficulties of measuring such low flow quantities in the intricate, microscopic lymphatic vessels.

This is the first study to model flow through a lymphatic valve using a fully-coupled ALE FSI method. The ALE method is advantageous because WSS values at the moving leaflet surface are readily obtained. This is possible through the remeshing algorithms implemented in the flow solver. Further, this model has revealed the presence of an eddy structure within the sinus adjacent to the valve leaflets throughout the entire wave cycle. These non-zero velocity values along instantaneous streamlines have not been observed in previous computational models of lymphatic valves, and have not been quantitatively identified through experimentation. Due to the highly compliant nature of the leaflets, which are thin elastin-based structures, modelling the movement of the valves through fully coupled fluid-structure interactions presents a significant computational challenge.

There were several limitations and simplifications in this study. One is the assumption of valve and vessel symmetry when constructing the ¼ model. Because of the low flow rates ($Re \approx 1$) within the lymphatic flow regime (Dixon, Greiner, Gashev, Cote, Moore Jr and

Zawieja 2006, Margaris, Nepiyushchikh, Zawieja, Moore Jr and Black 2016) it is not likely that slight asymmetries in leaflet geometry would greatly alter the flow patterns shown here. We have also not included the elasticity of the lymphatic vessel wall. Lymphatic vessel walls contain a high proportion of collagen (unlike the leaflets) and have highly nonlinear, strain-stiffening mechanical properties. This represents an additional challenge to the modelling, which will be addressed in future research. Additional limitations of this model include the constitutive model used to represent the leaflet material, which was neo-Hookean with shear and bulk moduli slightly less than that of arterial elastin (Mithieux and Weiss 2005, Nivison-Smith and Weiss 2011, Zou and Zhang 2009). Further studies should investigate non-homogeneity and variations in lymphatic leaflet material properties, including anisotropy. The exact material properties of lymphatic valve leaflets have not yet been characterized, but the properties used herein should fall within the physiologic range for mammalian lymphatic valves. And while an applied pressure of 44.5 Pa was sufficient to open the valve in these simulations, changing the material properties of the leaflets would undoubtedly change the response. Additionally, it has been observed that the amount of pressure required to open or close a valve depends on additional factors, including the transmural pressure and the level of vessel distention. Collagen buttresses at each side of the valve leaflets tether it to the vessel wall and allow the valve to open and close without inversion (Mazzoni, Skalak and Schmid-Schönbein 1987), suggesting that the motion of the vessel wall, due to passive distention or active contraction by LMCs, produces further complexity between wall motion, leaflet deflection, and lymph flow patterns which requires further investigation.

In conclusion, we have implemented a fully coupled FSI model of the rat mesenteric secondary lymphatic valve. This model allowed us to calculate the valve resistance to favorable pressure, an important parameter regulating lymphatic pumping. We also observed significant hysteresis during valve opening and closing. This calculated valve resistance presents the most

accurate estimation to date and can be used to update future models of lymphatic pumping, providing further insight into the complex fluid dynamics of the lymphatic system. A better understanding of lymphatic pumping is important in understanding basic physiological processes such as fluid balance and immune function. Pathologies involving lymphatic dysfunction (including valve malformation) include primary and secondary lymphedema, which is currently an incurable condition.

Acknowledgements

The authors gratefully acknowledge the following sources of support: The Royal Society, The Royal Academy of Engineering, The Sir Leon Bagrit Trust, and the United States National Institute of Health (NIH) Grant U01-HL-123420.

Declaration of Interests

The authors have no conflicting interests to declare.

References

Benoit JN, Zawieja DC, Goodman AH, Granger HJ. 1989. Characterization of intact mesenteric lymphatic pump and its responsiveness to acute edemagenic stress. American Journal of Physiology-Heart and Circulatory Physiology.257:H2059-H2069.

Bertram C, Macaskill C, Davis M, Moore Jr J. 2014. Development of a model of a multi-lymphangion lymphatic vessel incorporating realistic and measured parameter values. Biomechanics and modeling in mechanobiology.13:401-416.

Cao K, BukaČ M, Sucosky P. 2015. Three-dimensional macro-scale assessment of regional and temporal wall shear stress characteristics on aortic valve leaflets. Computer methods in biomechanics and biomedical engineering.1-11.

Cariati M, Bains S, Grootendorst M, Suyoi A, Peters A, Mortimer P, Ellis P, Harries M, Van Hemelrijck M, Purushotham A. 2015. Adjuvant taxanes and the development of breast cancer-related arm lymphoedema. British Journal of Surgery.102:1071-1078.

Chandran KB, Vigmostad SC. 2013. Patient-specific bicuspid valve dynamics: overview of methods and challenges. J Biomech. Jan 18;46:208-216.

Davis MJ, Rahbar E, Gashev AA, Zawieja DC, Moore JE. 2011. Determinants of valve gating in collecting lymphatic vessels from rat mesentery. American Journal of Physiology-Heart and Circulatory Physiology.301:H48-H60.

Dixon JB, Gashev AA, Zawieja DC, Moore Jr JE, Coté GL. 2007. Image correlation algorithm for measuring lymphocyte velocity and diameter changes in contracting microlymphatics. Annals of biomedical engineering.35:387-396.
Dixon JB, Greiner ST, Gashev AA, Cote GL, Moore Jr JE, Zawieja DC. 2006. Lymph flow, shear stress, and lymphocyte velocity in rat mesenteric prenodal lymphatics. Microcirculation.13:597-610.
Dixon JB, Zawieja DC, Gashev AA, Coté GL. 2005. Measuring microlymphatic flow using fast video microscopy. Journal of biomedical optics.10:064016-064016-064017.
Gordon KD, Mortimer PS. 2007. A guide to lymphedema. Expert Review of Dermatology.2:741-752.
Jamalian S, Bertram CD, Richardson WJ, Moore JE. 2013. Parameter sensitivity analysis of a lumped-parameter model of a chain of lymphangions in series. American Journal of Physiology-Heart and Circulatory Physiology.305:H1709-H1717.
Lantz J, Renner J, Karlsson M. 2011. Wall shear stress in a subject specific human aorta—influence of fluid-structure interaction. International Journal of Applied Mechanics.3:759-778.
Macdonald A. 2008. The computational modelling of collecting lymphatic vessels.
Margaris KN, Nepiyushchikh Z, Zawieja DC, Moore Jr JE, Black R. 2016. Microparticle image velocimetry approach to flow measurements in isolated contracting lymphatic vessels. Journal of Biomedical Optics.21.
Marom G, Haj-Ali R, Raanani E, Schäfers H-J, Rosenfeld M. 2012. A fluid–structure interaction model of the aortic valve with coaptation and compliant aortic root. Medical & biological engineering & computing.50:173-182.
Mazzoni M, Skalak T, Schmid-Schönbein G. 1987. Structure of lymphatic valves in the spinotrapezius muscle of the rat. Journal of Vascular Research.24:304-312.
Mellor RH, Brice G, Stanton AW, French J, Smith A, Jeffery S, Levick JR, Burnand KG, Mortimer PS. 2007. Mutations in FOXC2 are strongly associated with primary valve failure in veins of the lower limb. Circulation.115:1912-1920.
Mithieux SM, Weiss AS. 2005. Elastin. Advances in protein chemistry.70:437-461.
Mortimer PS, Rockson SG. 2014. New developments in clinical aspects of lymphatic disease. The Journal of clinical investigation.124:915-921.
Nivison-Smith L, Weiss A. 2011. Elastin based constructs: INTECH Open Access Publisher.
Rahbar E, Weimer J, Gibbs H, Yeh AT, Bertram CD, Davis MJ, Hill MA, Zawieja DC, Moore Jr JE. 2012. Passive pressure–diameter relationship and structural composition of rat mesenteric lymphangions. Lymphatic research and biology.10:152-163.
Sabine A, Bovay E, Demir CS, Kimura W, Jaquet M, Agalarov Y, Zangger N, Scallan JP, Graber W, Gulpinar E. 2015. FOXC2 and fluid shear stress stabilize postnatal lymphatic vasculature. The Journal of clinical investigation.125:3861.
Swartz MA, Fleury ME. 2007. Interstitial flow and its effects in soft tissues. Annu Rev Biomed Eng.9:229-256.
Swartz MA, Skobe M. 2001. Lymphatic function, lymphangiogenesis, and cancer metastasis. Microscopy research and technique.55:92-99.
Takada M. 1971. The ultrastructure of lymphatic valves in rabbits and mice. American Journal of Anatomy.132:207-217.
Vajda J, Tomcsik M. 1971. The structure of the valves of the lymphatic vessels. Cells Tissues Organs.78:521-531.
Wilson JT, van Loon R, Wang W, Zawieja DC, Moore JE. 2015. Determining the combined effect of the lymphatic valve leaflets and sinus on resistance to forward flow. Journal of biomechanics.48:3584-3590.
Wilson JT, Wang W, Hellerstedt AH, Zawieja DC, Moore JE. 2013. Confocal image-based computational modeling of nitric oxide transport in a rat mesenteric lymphatic vessel. Journal of biomechanical engineering.135:051005.
Zawieja DC, von der Weid PY, Gashev AA. 2011. Microlymphatic biology. Comprehensive Physiology.

Zou Y, Zhang Y. 2009. An experimental and theoretical study on the anisotropy of elastin network. Annals of biomedical engineering.37:1572-1583.

Table 1. (column width)

Description	*Symbol*	*Value, Units*
Maximum diameter of the sinus area	D_{max}	160 µm
Height from the root of the commissural incissura measured in the axial direction	H_c	240 µm
Height from the root to the trailing edge	H_{te}	136 µm
Length from root to maximum diameter	H_{md}	217 µm
Length of the total sinus region	H_s	434 µm
Diameter of the elliptic orifice	d_o	10 µm
Diameter of root	D_r	100 µm
Sinus-to-root ratio	*STR*	1.6
Leaflet thickness	*h*	5 µm

Table 1. Geometrical parameters used to construct the lymphatic valve leaflets and sinus. See reference (Wilson, van Loon, Wang, Zawieja and Moore 2015) for a description on how the idealized geometry is generated from these parameters.

Table 2. (column width)

Parameter	*Value, Units*
Minimum Length Scale	0.21 µm
Maximum Length Scale	22 µm
Maximum Cell Skewness	0.95
Maximum Face Skewness	0.9
Size Remeshing Interval	1

Table 2. Remeshing parameters used in FSI simulations.

Figure 1. (column width)

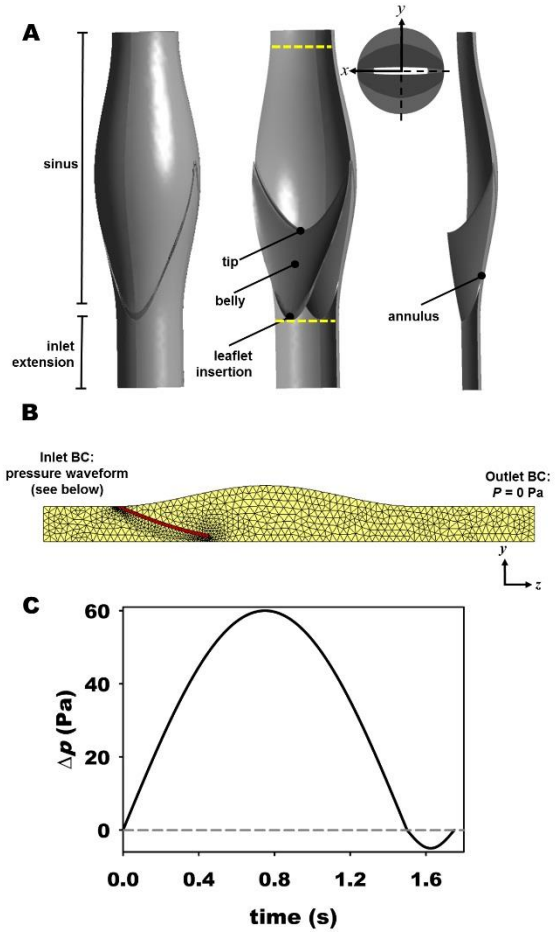

Figure 1. Model geometry, mesh, and pressure boundary conditions (A) 3D views of the lymphatic valve and sinus geometry. On the left is the full geometry, in the middle is the full geometry with the outer vessel wall made transparent to visualize the valve, and on the right is the ¼-symmetry model. Note that the outlet extension is not shown. A 'down-the-barrel' view of the valve is also included to illustrate the coordinate system and lines of symmetry applied to the model. The *z*-axis was defined along the length of the vessel, running from inlet to outlet. The *x*-axis was oriented along the major axis of the elliptical orifice of the valve, and the *y*-axis was oriented along the minor axis of the orifice. Symmetry was applied along the *xz*- and *yz*-plane to create the ¼-symmetry model. The yellow dashed lines indicate the location of the upstream and downstream planes used to calculate resistance. (B) The computational mesh of

the fluid domain (yellow) and the solid leaflet domain (red). Inlet pressure was prescribed as a waveform (see below) while outlet pressure was maintained at 0 Pa. (C) Dynamic pressure waveform imposed at the inlet of the fluid domain. Transvalvular pressure reached a maximum of 60 Pa at 0.75 s, and a minimum of -5 Pa at 1.625 s.

Figure 2. (page width)

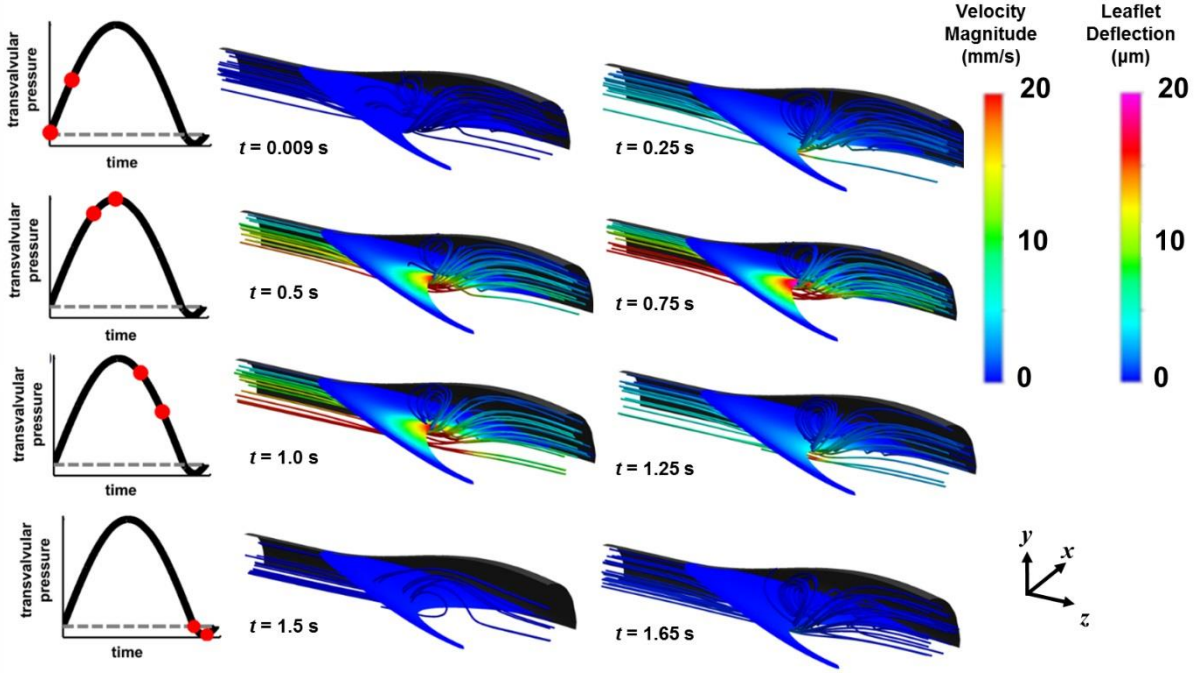

Figure 2. Snapshots of instantaneous velocity streamlines and contours of leaflet deflection at eight time points. The sampling times are indicated by the red circles overlaid on the waveform on each row; numerical values of the time points are shown below each case.

Figure 3. (page width)

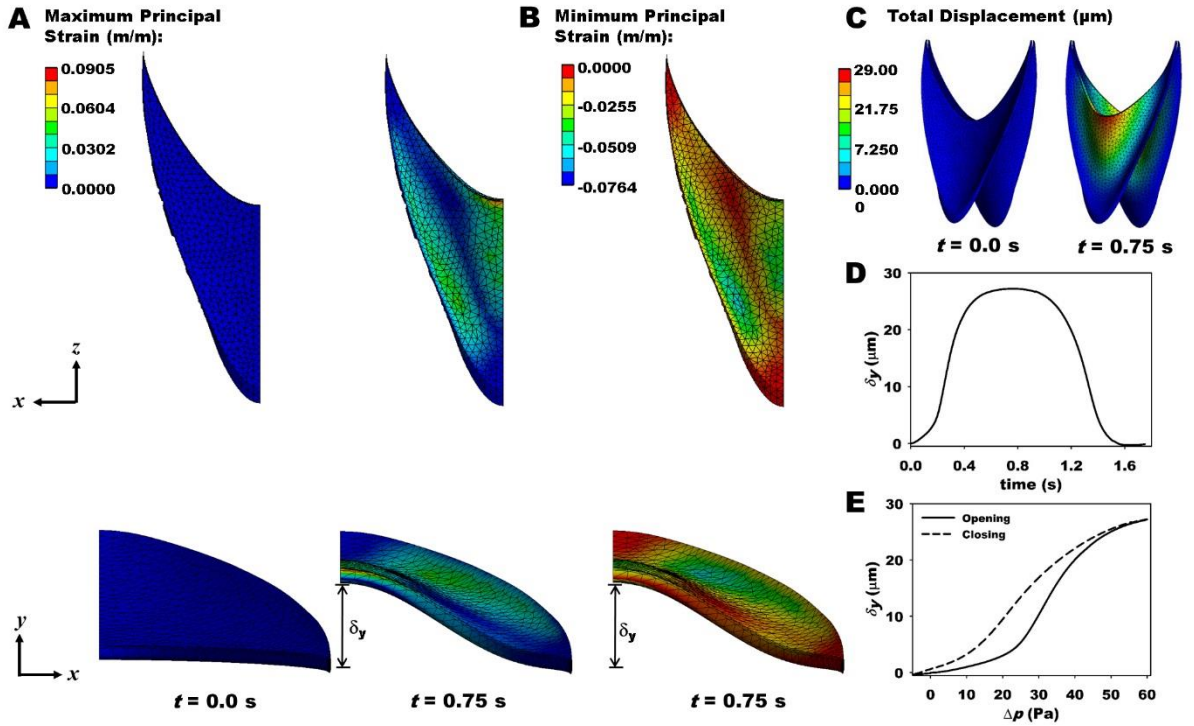

Figure 3. Strain and deflection of the solid leaflet due to increasing lymph flow. (A) The ¼ symmetry representation of the valve leaflet at the initial configuration (t = 0.0 s, left) and at peak inlet pressure (t = 0.75 s, right). Maximum principal strain indicates that the areas with the most positive strain occurred along the upper surface of the deflected orifice and along the boundary with the vessel wall. (B) Minimum principal strain was also concentrated along the same areas of the leaflet. (C) Full geometry reconstruction of the valve at the initial configuration and at max inlet pressure. The fringe plot indicates total displacement of the leaflet. (D) Tip deflection versus time. Deflection of the leaflet tip in the y-direction, δ_y, which was perpendicular to axial lymph flow. This deflection can also be thought of as the change in the minor axis of the elliptical orifice of the valve, while the major axis (x-direction) remains constant. (E) Tip deflection versus transvalvular pressure during the opening (solid line) and closing (dashed line) of the valve.

Figure 4. (page width)

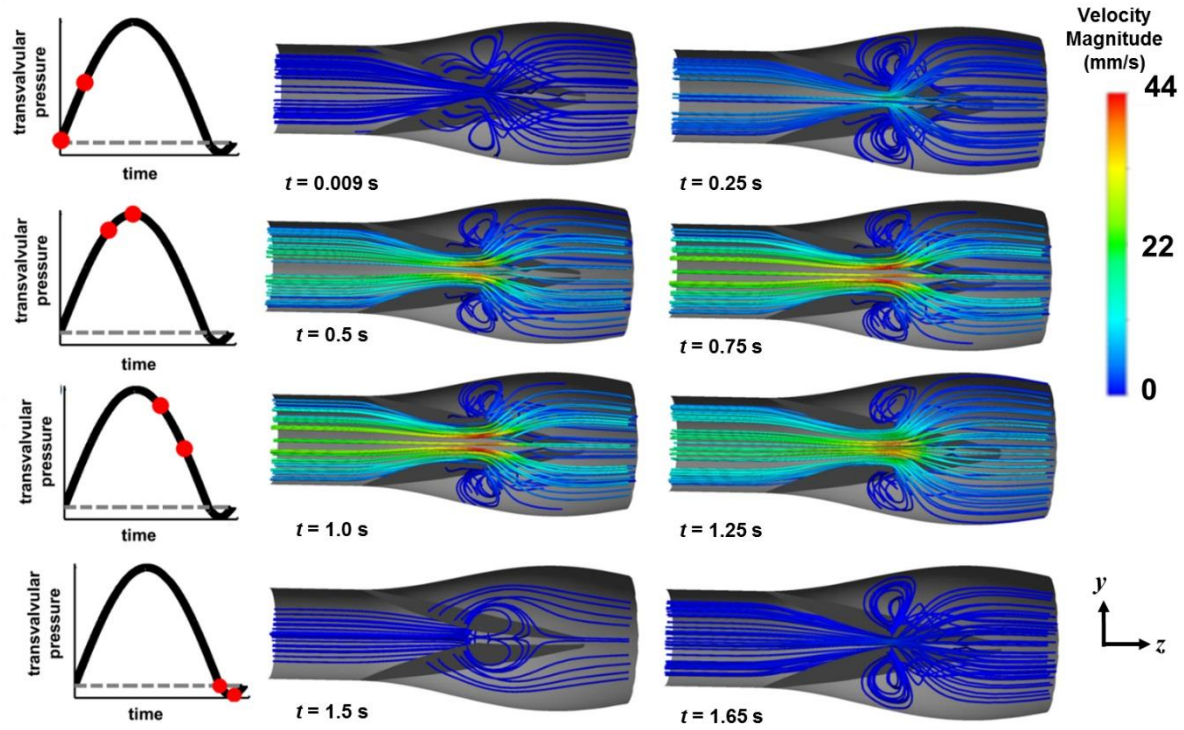

Figure 4. Leaflet profile and instantaneous velocity streamlines. Velocity streamlines are represented as tubular ribbons to show fluid particle paths. Regions of apparent recirculation are present across all time points sampled. The sampling times are indicated by the red circles overlaid on the waveform on each row; numerical values of the time points are shown below each case.

Figure 5. (column width)

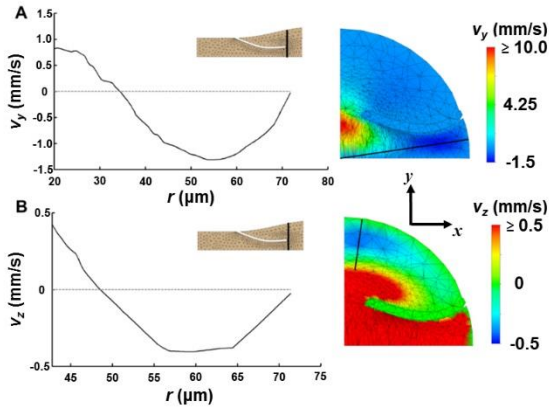

Figure 5. Velocity components in the *y*-direction, v_y (A), and axial direction, v_z (B), sampled on two radial planes (locations are shown in contours at the right of each plot). The *x*- and *y*-directions are indicated on the coordinate axis, and the *z*-direction points out of the paper (axis of the vessel). Beige-colored insets of the valve geometry within each plot show the axial locations of the sampling probes immediately downstream of the leaflet tip. v_y has a minimum value of -1.32 mm/s and v_z has a minimum value of -0.41 mm/s.

Figure 6. (column width)

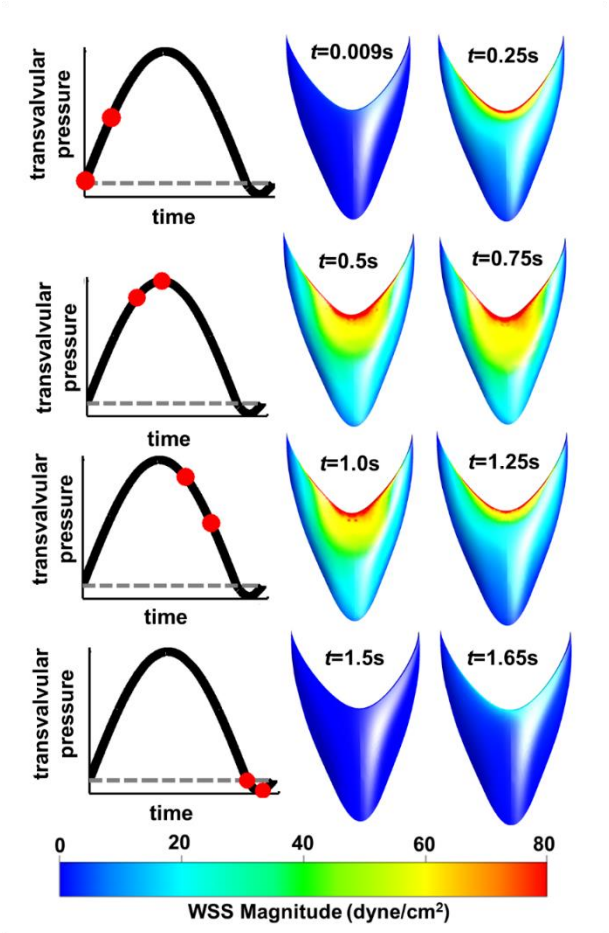

Figure 6. WSS magnitude sampled on the leaflet surface exposed to central lymph flow. The sampling times are indicated by the red circles overlaid on the waveform on each row.

Figure 7. (column width)

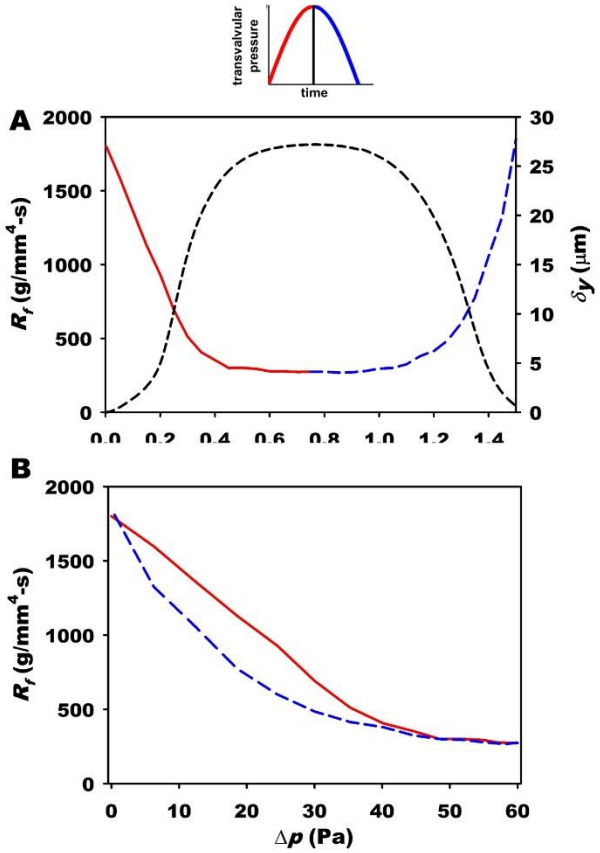

Figure 7. Resistance to favorable pressure, R_f, was calculated from the pressure drop across the valve divided by the flow rate downstream of the valve. Panel (A) shows the resistance versus time, while panel (B) shows the resistance verses transvalvular pressure. Resistance during the opening of the valve is shown in red (t = 0 to t = 0.75 s), and resistance during closing is shown in blue (t = 0.75 to t = 1.5 s). The black dashed line and right axis in panel (A) show leaflet tip deflection for the same time-period, as shown in Fig. 3. The computed minimum valve resistance to favorable pressure is 268 g/mm^4-s at 0.846 s. Note that resistance values where a negative transvalvular pressure was applied at the inlet which reversed the direction of flow are not shown.